Hydride Reduction of BaTiO3 ? Oxyhydride Versus O Vacancy Formation

(article starts on next page)

# Hydride Reduction of BaTiO₃ − Oxyhydride Versus O Vacancy Formation

Reji Nedumkandathil,[†] Aleksander Jaworski,[†] Jekabs Grins,[†] Diana Bernin,[‡] Maths Karlsson,[‡] Carin Eklöf-Österberg,[‡] Alexandra Neagu,[†] Cheuk-Wai Tai,[†] Andrew J. Pell,[†] and Ulrich Häussermann*,[†]

[†]Department of Materials and Environmental Chemistry, Stockholm University, SE-10691 Stockholm, Sweden
[‡]Department of Chemistry and Chemical Engineering, Chalmers University of Technology, SE-41296 Gothenburg, Sweden

Ⓢ Supporting Information

ABSTRACT: We investigated the hydride reduction of tetragonal $BaTiO_3$ using the metal hydrides CaH_2, NaH, MgH_2, $NaBH_4$, and $NaAlH_4$. The reactions employed molar $BaTiO_3$/H ratios of up to 1.8 and temperatures near 600 °C. The air-stable reduced products were characterized by powder X-ray diffraction (PXRD), transmission electron microscopy, thermogravimetric analysis (TGA), and ^1H magic angle spinning (MAS) NMR spectroscopy. PXRD showed the formation of cubic products—indicative of the formation of $BaTiO_{3−x}H_x$—except for NaH. Lattice parameters were in a range between 4.005 Å (for $NaBH_4$-reduced samples) and 4.033 Å (for MgH_2-reduced samples). With increasing H/$BaTiO_3$ ratio, CaH_2-, $NaAlH_4$-, and MgH_2-reduced samples

were afforded as two-phase mixtures. TGA in air flow showed significant weight increases of up to 3.5% for reduced $BaTiO_3$, suggesting that metal hydride reduction yielded oxyhydrides $BaTiO_{3−x}H_x$ with x values larger than 0.5. ^1H MAS NMR spectroscopy, however, revealed rather low concentrations of H and thus a simultaneous presence of O vacancies in reduced $BaTiO_3$. It has to be concluded that hydride reduction of $BaTiO_3$ yields complex disordered materials $BaTiO_{3−x}H_y\square_{(x−y)}$ with x up to 0.6 and y in a range 0.04−0.25, rather than homogeneous solid solutions $BaTiO_{3−x}H_x$. Resonances of (hydridic) H substituting O in the cubic perovskite structure appear in the −2 to −60 ppm spectral region. The large range of negative chemical shifts and breadth of the signals signifies metallic conductivity and structural disorder in $BaTiO_{3−x}H_y\square_{(x−y)}$. Sintering of $BaTiO_{3−x}H_y\square_{(x−y)}$ in a gaseous H_2 atmosphere resulted in more ordered materials, as indicated by considerably sharper ^1H resonances.
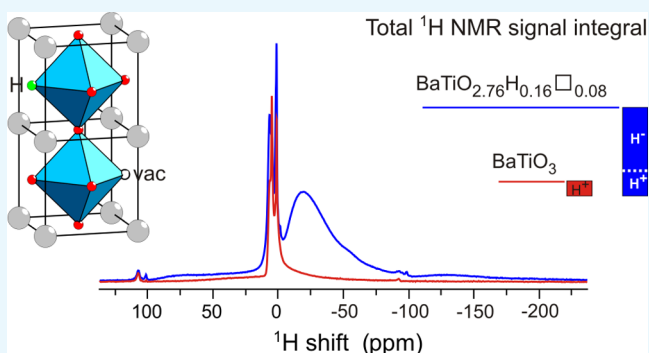
1. INTRODUCTION

Hydride reduction has developed into a versatile method for modifying transition metal oxides, yielding highly reduced products with unusual coordination environments and exotic electronic and magnetic properties.[1−4] Especially fruitful precursors are oxides that relate to perovskite and Ruddlesden−Popper phases. Specific prominent examples are the $LaNiO_3$ to $LaNiO_2$, $SrFeO_3$ to $SrFeO_2$, and $YBaCo_2O_5$ to $YBaCo_2O_{4.5}$ reductions.[5−7] In a typical hydride reduction, a ternary transition metal oxide is reacted with CaH_2, NaH, or LiH at relatively mild, low temperature ("chimie douce") conditions (150−600 °C). The reduction is accompanied with O removal (i.e., O vacancy formation), and frequently, there is a strict topotactic relationship between the original oxide and its reduced form. In rare cases, transition metal reduction and hydride ion insertion occur simultaneously, leading to oxyhydrides.[8] This scenario is thought to be highly unusual because of the incompatibility of $O^{2−}$ and strongly reducing $H^−$ in forming a common anion substructure.[9]

It then came as a surprise when in 2012 Kobayashi et al. reported that the reaction of CaH_2 with the archetypical perovskite $BaTiO_3$ affords $BaTiO_{3−x}H_x$ with large amounts ($x < 0.6$) of hydrogen incorporated.[10] The cubic perovskite oxyhydride $BaTiO_{3−x}H_x$ is remarkable in several respects. It represents a defect-/vacancy-free solid solution of $O^{2−}$ and $H^−$ ions, which commonly form the octahedral environment around Ti that is now in a mixed IV/III oxidation state (Figure 1a). $BaTiO_{3−x}H_x$ is stable in air and water. Further, it is stable at elevated temperatures of up to approximately 400 °C above which hydrogen is released. When present, oxygen is scavenged and $BaTiO_3$ is retained. In inert gas atmospheres containing D_2, a hydride exchange H/D occurs at hydrogen release temperatures. Also, oxynitrides $BaTiO_{3−δ}N_y$ may be prepared by heating $BaTiO_{3−x}H_x$ under N_2 flow at 400−600
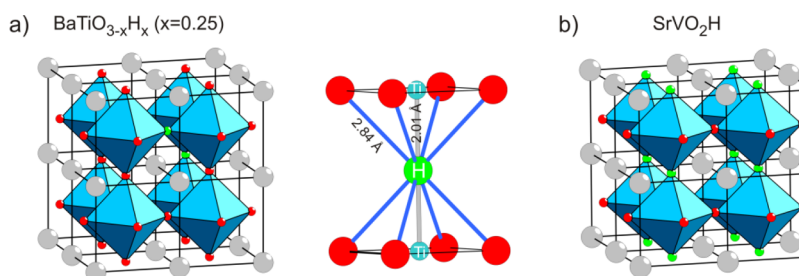
Figure 1. (a) Structure of $BaTiO_{2.75}H_{0.25}$ represented as the $2 \times 2 \times 2$ supercell of cubic $BaTiO_3$ in which two O atoms were randomly replaced by two H atoms. The right-hand side shows the local coordination of H in $BaTiO_{3-x}H_x$. The Ti is in a mixed IV/III oxidation state. (b) Anion-ordered tetragonal structure of $SrVO_2H$.[15] The alkaline earth metal, O, and H atoms are depicted as gray, red, and green spheres, respectively.

°C.[11] These observations led to the conclusion that the hydride species in $BaTiO_{3-x}H_x$ is labile and that the material represents a versatile precursor toward new mixed-anion compounds.[12] Sakaguchi et al.[13] and Yamamoto et al.[14] showed that perovskite oxyhydrides are also obtained with $CaTiO_3$, $SrTiO_3$, and $EuTiO_3$ although with smaller hydride contents x (<0.3). A high degree of O^{2-}/H^- exchange was further observed for cubic $SrVO_3$ for which topochemical hydride reduction with CaH_2 yields tetragonal $SrVO_2H$.[15] Remarkably, the structure of $SrVO_2H$ is fully anion-ordered, displaying two-dimensional VO_2 sheets that are connected by H^- ligands (cf. Figure 1b).

Mechanisms or processes behind metal hydride reductions are not well investigated and far from understood. They involve intermediates, which in turn depend on the particular system and conditions applied. Also, the active reducing species may be H^- or H_2 or a combination of both. Hayward et al. could show that the reduction of $LiNiO_3$ with NaH corresponds to a solid-state diffusion-controlled reaction that proceeds via the intermediate $LaNiO_{2+x}$.[5] For other systems, there may be significant H_2 gas-phase contributions to reduction.[16] Conditions can be varied by the choice of reducing agents (i.e., metal hydride), reaction temperature and time, and the activity/concentration of H^-. Hernden et al. performed a comprehensive investigation of the hydride reduction of Sr_2MnO_4 and identified a two-electron transfer $H^- \rightarrow H^+$ (as opposed to one-electron transfer $H^- \rightarrow 1/2H_2$) during reduction.[17] For oxyhydride formation, additional complexity arises. Are reduction and exchange mechanisms coupled, or does oxyhydride formation occur via an O vacancy-rich intermediate? Bridges et al. studied the formation pathway of the first reported transition metal oxyhydride $LaSrCoO_3H_{0.7}$ from $LaSrCoO_4$.[18] From in situ X-ray diffraction studies, they could identify oxygen-deficient $LaSrCo_3O_{3.38-x}$ as the reduced intermediate, in which oxide was subsequently substituted by H^-. At the same time, the presence of gas-phase H_2 appeared to be important for achieving the final composition $LaSrCo_3H_{0.7}$. The proposed three-step mechanism is rather complex, but it is clear that direct hydride substitution for oxide, coupled with reduction, is excluded.

An important question is what factors govern oxyhydride formation as opposed to exclusive vacancy formation during hydride reduction. What mechanism could apply for $BaTiO_3$ reduction? Whereas defined reduced phases can be obtained from $LaSrCoO_4$ (i.e., $LaSrCoO_{3.50}$ and $LaSrCoO_{3.38}$),[18] $BaTiO_{3-x}$ with significant O deficiency is not known. We report a systematic study of the hydride reduction of $BaTiO_3$, especially investigating the influence of reducing agents. In contrast to previous studies, we find that hydride reduction

leads to phases $BaTiO_{3-x}H_y\square_{(x-y)}$ with comparatively low H content and, accordingly, large O vacancy concentrations.

2. EXPERIMENTAL METHODS

2.1. Synthesis. As starting materials, we used $BaTiO_3$ (500 nm particle size, 99.9% purity, ABCR GmbH) and powders of the metal hydrides CaH_2 (99.99%, Sigma-Aldrich), NaH (95%, Sigma-Aldrich), MgH_2 (96.5%, Sigma-Aldrich), $NaBH_4$ (98%, ABCR GmbH), and $NaAlH_4$ (93%, Sigma-Aldrich). Prior to use, $BaTiO_3$ was dried overnight in an oven at 200 °C. All steps of sample preparation for the synthesis reactions were performed in an Ar-filled glovebox. For a typical synthesis, ~1.4 g (6 mmol) of $BaTiO_3$ was intimately mixed with metal hydride by grinding the materials together in an agate mortar for 15 min. We considered the molar proportions $BaTiO_3$ + nH, with n = 0.2, 0.6, 1.2, and 1.8 and with H = NaH, 0.5 CaH_2, 0.5 MgH_2, 0.25 $NaAlH_4$, and 0.25 $NaBH_4$. Samples are in the following termed "n-H-MH_n", to indicate the hydride concentration and hydride source (M = Na, Ca, Mg, "NaAl", "NaB") in the reaction. The $BaTiO_3/MH_n$ mixture was subsequently pressed into a pellet with a diameter of 8 mm. The pellet was then sealed inside a stainless steel ampule (with dimensions 10 mm ID and 80 mm length), which in turn was placed in a fused silica jacket.

Following removal from the glovebox, the silica jacket was placed in a vertical tube furnace and connected to a vacuum line. The empty space of the furnace was filled with silica insulation wool, and a K-type thermocouple was introduced parallel to the silica jacket to monitor the temperature close to the location of the metal ampule. The silica jacket was then evacuated, and ampules were heated for times between 1 and 7 days. Reaction temperatures were varied from 500 to 700 °C. Most reactions reported in this work were carried out at 600 °C in 2 days' duration. A deuterated sample 1.2-D-CaD_2 was prepared by reacting a mixture of $BaTiO_3$ and CaD_2 at 600 °C for 2 days. CaD_2 was synthesized prior by reacting dendritic pieces of Ca (99.99% trace metals purity, Sigma-Aldrich) with D_2 (99.9% isotope purity, AGA) in a stainless-steel autoclave pressurized to 30 bar at 400 °C for 12 h.

Products were washed with 0.1 M CH_3COOH (HAc) to remove excess metal hydride and metal oxide formed during hydride reduction and dried at 120 °C under dynamic vacuum (<10^{-5} bar). In order to study the effect of the acidic washing agents, we also used a 0.1 M NH_4Cl/methanol (MeOH) mixture and 0.1 M HCl. For washing, the pellets were crushed and sonicated with 50 mL acidic washing agent for 15 min and then centrifuged. The procedure was repeated three times. As a last step, samples were treated with 20 mL of pure methanol.

Selected reduced $BaTiO_3$ samples were subjected to a posttreatment in which the pellets were heated in a corundum crucible in a stainless steel autoclave at 600 °C under a pressure of 30−50 bar of hydrogen gas (H_2 AGA 99.99% purity) for 24 h.

2.2. Powder X-ray Diffraction (PXRD) Analysis. Ambient-temperature PXRD patterns were collected on a PANalytical X'Pert PRO diffractometer operated with Cu Kα_1 radiation in θ−2θ diffraction geometry. Powder samples were mounted on a Si wafer zero-background holder, and diffraction patterns were measured in a 2θ range of 10−90° with 0.013° step size. In situ high-temperature PXRD studies were performed on a PANalytical X'Pert PRO instrument with Cu Kα radiation in θ−2θ diffraction geometry. Samples were heated in air to 900 °C using an Anton Paar XRK 900 high-temperature chamber equipped with Be windows and connected to a temperature controller. Powder samples were mounted on a Au wafer. Data in a 2θ range of 20−60° were collected at room temperature and then in steps of 100 °C with 15 min acquisition time and 5 °C/min heating rate between the steps. Au reflections were used for correction of the 2θ-scale of data. The contribution of Kα_2 radiation to the PXRD patterns was removed using the PANalytical X'Pert HighScore Plus software. The Rietveld method as implemented in the FullProf program was used for structure and phase analysis.[19] A six-coefficient polynomial function was applied for the background. The peak shape was described by a pseudo-Voigt function. Patterns with pronounced peak shape asymmetries were refined as mixtures of two cubic phases. Site occupancies for the O atoms could not be refined reliably and were constrained to 1.

2.3. Transmission Electron Microscopy (TEM) Investigations. The TEM images were recorded using either a JEOL JEM-2100F (C_s = 0.5 mm and point resolution of 1.9 Å) or a JEOL JEM-2100 microscope (C_s = 1.4 mm and point resolution 2.5 Å). Both microscopes were operated at room temperature with an accelerating voltage of 200 kV. The TEM specimens were prepared by crushing the dry powders in an agate mortar, followed by dispersion in ethanol. One droplet of this suspension was transferred onto a copper grid coated with a holey-carbon film.

2.4. Thermogravimetric Analysis (TGA). TGA experiments were carried out using a TA instruments Discovery system. The samples (∼15 mg powders) were heated in a platinum crucible from room temperature to 900 °C with a heating rate of 5 °C/min. A dry air gas flow of 20 mL/min was applied.

2.5. Magic Angle Spinning (MAS) NMR Spectroscopy. The ^{1}H MAS NMR experiments were performed at a magnetic field of 14.1 T (600.12 MHz ^{1}H Larmor frequency) and a MAS frequency of 60 kHz on a Bruker AVANCE-III spectrometer equipped with a 1.3 mm MAS HX probe. Spectra were acquired using a rotor-synchronized, double-adiabatic spin-echo sequence with a 1.2 μs 90° excitation pulse length, followed by a pair of 50 μs tanh/tan short high-power adiabatic pulses (SHAPs) with 5 MHz frequency sweep.[20−22] All pulses were applied at a nutation frequency of 208 kHz. Signal transients (4096) with a 5 s recycle delay were accumulated for each sample. The shifts were referenced with respect to tetramethylsilane (TMS) at 0 ppm. The ^{2}H MAS NMR spectrum was recorded on a 9.4 T (61.41 MHz ^{2}H Larmor frequency) Bruker AVANCE-III spectrometer with a 2.5 mm MAS HX probe at a spinning frequency of 30 kHz.

The same pulse sequence as for protons was used but with a 3.0 μs 90° excitation pulse and 66.67 μs SHAPs at a nutation frequency of 83 kHz. Scans (4096) with a 20 s recycle delay were collected. The shifts were referenced to deuterated TMS (TMS-d_{12}) at 0 ppm.
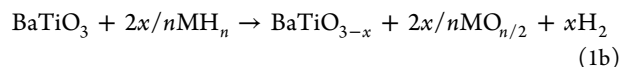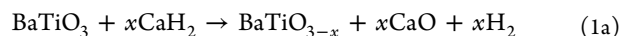
3. RESULTS AND DISCUSSION

3.1. Hydride Reduction of $BaTiO_3$. Kobayashi et al. prepared $BaTiO_{3−x}H_x$ by reacting $BaTiO_3$ in the form of 170 nm sized particles with CaH_2 at temperatures between 500 and 580 °C for 4−7 days in pyrex or fused silica tubes.[10,13] CaH_2 was employed with a rather large excess, 3 M, corresponding to 6 H according to our nomenclature. The reacted samples were washed with 0.1 M NH_4Cl/MeOH in air to remove excess CaH_2 as well as the side product CaO. Very weakly acidic NH_4Cl/MeOH is commonly used as a washing agent for concluding hydride reductions.[1−4] The dark blue-colored cubic products were identified as $BaTiO_{3−x}H_x$ and described as a defect-free $O^{2−}$/$H^−$ solid solution containing xTi(III) and 1−xTi(IV) with x up to 0.6.

In the following, we outline possible processes that occur during the hydride reduction of $BaTiO_3$. The $H^−$ species as a reductant may transfer one or two electrons toward oxygen vacancy formation ("one-" and "two"-electron processes, respectively). In addition, the metal hydride may decompose at elevated temperatures into hydrogen gas and metal, which can both act as reductants. H_2 gas-phase contribution to hydride reduction reactions has been demonstrated by Kobayashi et al.[16] For oxyhydride formation, $H^−$ formally acts by simultaneously reducing Ti and replacing $O^{2−}$ in the perovskite structure. However, the reaction may proceed via initial vacancy formation and subsequent oxidation by gaseous H_2. Processes involving hydrogen are summarized in Table 1. Additionally, the explicit hydride reduction reactions for $BaTiO_3$ are formulated below for CaH_2 (a) and for a generic metal hydride MH_n (b).
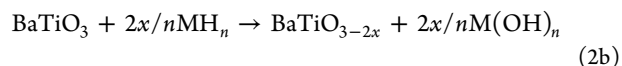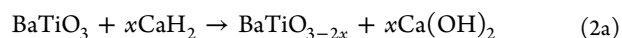
Table 1. Processes Involving Hydrogen Species during Hydride Reduction

process	oxidation	side products
vacancy, 1e	$H^− \rightarrow H^\bullet + e$	$0.5(O^{2−} + H_2)$
vacany, 2e	$H^− \rightarrow H^+ + 2e$	$OH^−$
H_2, gas phase	$H^\bullet \rightarrow H^+ + e$	$0.5H_2O$
oxyhydride formation	$2H^− \rightarrow H^− + H^\bullet + e$	$0.5(O^{2−} + H_2)$

Vacancy formation, one-electron process

$$BaTiO_3 + xCaH_2 \rightarrow BaTiO_{3−x} + xCaO + xH_2 \qquad (1a)$$

$$BaTiO_3 + 2x/nMH_n \rightarrow BaTiO_{3−x} + 2x/nMO_{n/2} + xH_2 \qquad (1b)$$

Vacancy formation, two-electron process

$$BaTiO_3 + xCaH_2 \rightarrow BaTiO_{3−2x} + xCa(OH)_2 \qquad (2a)$$

$$BaTiO_3 + 2x/nMH_n \rightarrow BaTiO_{3−2x} + 2x/nM(OH)_n \qquad (2b)$$

Vacancy formation, H_2

$$BaTiO_3 + xH_2 \rightarrow BaTiO_{3−x} + xH_2O$$
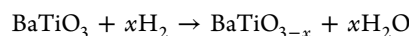
Oxyhydride formation, direct substitution

$$BaTiO_3 + xCaH_2 \rightarrow BaTiO_{3-x}H_x + xCaO + x/2H_2 \tag{3a}$$

$$BaTiO_3 + 2x/nMH_n$$
$$\rightarrow BaTiO_{3-x}H_x + 2x/nMO_{n/2} + x/2H_2 \tag{3b}$$
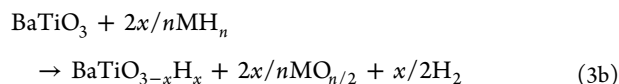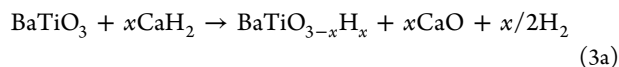
Oxyhydride formation, via a defect intermediate

$$BaTiO_{3-x} + x/2H_2 \rightarrow BaTiO_{3-x}H_x$$
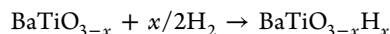
Note that if hydroxide is formed (two-electron process), it may most likely not be observed in the ex situ analysis of products because hydroxide will react with excess hydride to yield oxide and H_2 ($OH^- + H^- \rightarrow O^{2-} + H_2$).

3.2. Reduction with CaH_2. Our reactions were performed at 600 °C in welded stainless steel ampules. The average particle size of the $BaTiO_3$ starting material was 500 nm, which is slightly larger than the material used by Kobayashi et al. Products were washed with 0.1 M HAc, which expedited the procedure considerably compared to the much less acidic NH_4Cl/MeOH. From PXRD, TGA, and ^1H NMR measurements, we concluded that the products after washing with 0.1 M HAc and 0.1 M NH_4Cl/MeOH were identical (see the Supporting Information, part III). Figure 2 shows the evolution of products with increasing CaH_2 concentration during 2 day experiments at 600 °C, and Table 2 presents the results from the refinement of the PXRD patterns. The product obtained with 0.2 H ("0.2-H-CaH_2") had a pale blue color and remained tetragonal. With the higher concentrations, 0.6, 1.2, and 1.8 H cubic products were obtained. A higher degree of reduction with increasing H concentration was recognizable by a deepening of the color to dark blue, almost black, in agreement with the observation of Kobayashi et al.[10,13] The unit cell volume of the reduced products is very similar to that of the starting material, increasing slightly with increasing H concentration. A closer inspection of the PXRD patterns of 1.2-H-CaH_2 and 1.8-H-CaH_2 revealed that reflections have a pronounced shoulder at lower angles, suggesting phase heterogeneity. These patterns were refined as a mixture of two cubic phases. For both products, the minority phase had a weight fraction of about 11% and a unit cell parameter that was larger than that of the majority phase by about 0.014 Å. We note that the lattice parameter reported by Kobayashi et al. for $BaTiO_{2.38}H_{0.62}$, 4.0236 Å,[10] is similar to the minority phase of the 1.2-H-CaH_2 and 1.8-H-CaH_2 samples. Higher concentrations than 1.8 H led to a drastic broadening of reflections and a diminished crystallinity.

The presence of two cubic phases in the 1.2-H-CaH_2 and 1.8-H-CaH_2 samples, as evidenced from PXRD, could not be reconciled from TEM investigations. Figure 3a,b shows TEM images of the starting material and 1.2-H-CaH_2, respectively. The morphology of the crystalline particles is not influenced by the hydride reduction reaction. The electron diffraction pattern of investigated 1.2-H-CaH_2 crystallites, shown in Figure 3c, is cubic without signs of superstructuring or diffuse scattering. However, the thickness of the crystallites hampered detailed diffraction studies.

Kobayashi et al. suggested that TGA represents a convenient way to assess the H content of $BaTiO_{3-x}H_x$.[10,13] TGA under the flowing air will monitor the reaction

$$BaTiO_{3-x}H_x + 0.75xO_2 \rightarrow BaTiO_3 + 0.5xH_2O \tag{4}$$
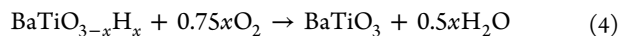
according to which a substantial weight increase occurs, and thus, a high accuracy can be associated with the determination
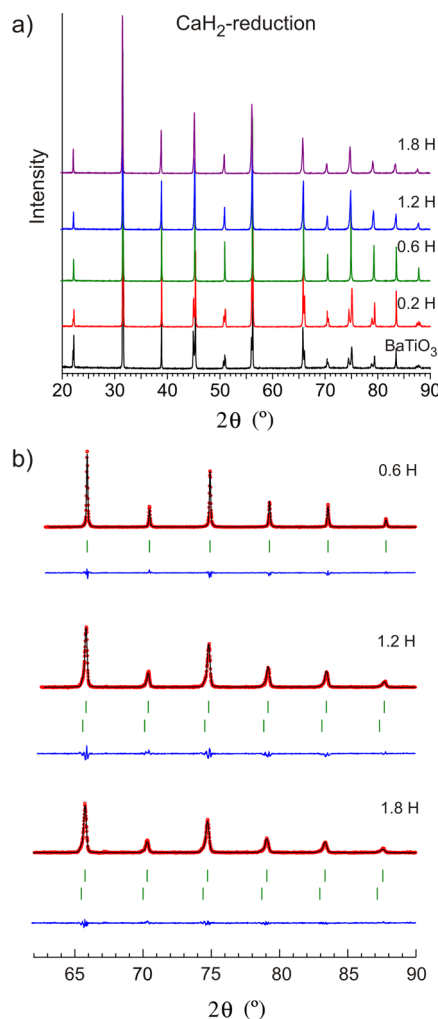

Figure 2. (a) PXRD patterns of products obtained from the hydride reduction of $BaTiO_3$ at 600 °C during 2 days, using various concentrations of CaH_2. (b) Rietveld plots for the PXRD patterns of the samples obtained with 0.6, 1.2, and 1.8 H concentrations of CaH_2 showing the evolution of two-phase mixture with increasing H concentration.

Table 2. Synthesis Products from Hydride Reduction with CaH_2 during 2 Day Experiments at 600 °C

sample	product/fraction (wt %)	lattice parameters (Å)	volume (Å³)	x from TG[a]
0-H	tetragonal	a = 3.9964(1), c = 4.0310(1)	64.379(2)	0
0.2-H	tetragonal	a = 3.9971(1), c = 4.0260(1)	64.324(3)	0.03
0.6-H	cubic	4.0051(6)	64.247(2)	0.10
1.2-H	cubic-I/89(1)	4.0096(2)	64.461(2)	0.24
	cubic-II/11(1)	4.0219	65.095	
1.8-H	cubic-I/89(1)	4.0138(1)	64.662(2)	0.34
	cubic-II/11(1)	4.0288	65.391	

[a]x refers to a reaction $BaTiO_{3-x}H_x + 0.75xO_2 \rightarrow BaTiO_3 + 0.5xH_2O$.

of x. The product after TGA (i.e., after heating and cooling to 900 °C) is white and corresponds to tetragonal $BaTiO_3$. Figure 4 collects the TGA traces for the CaH_2-reduced samples. All samples show initially a small weight loss (0.1–0.15%) which we attribute to the loss of surface water/hydroxyls. For the 0.2-H-CaH_2 sample, the weight loss continued up to 600 °C, for
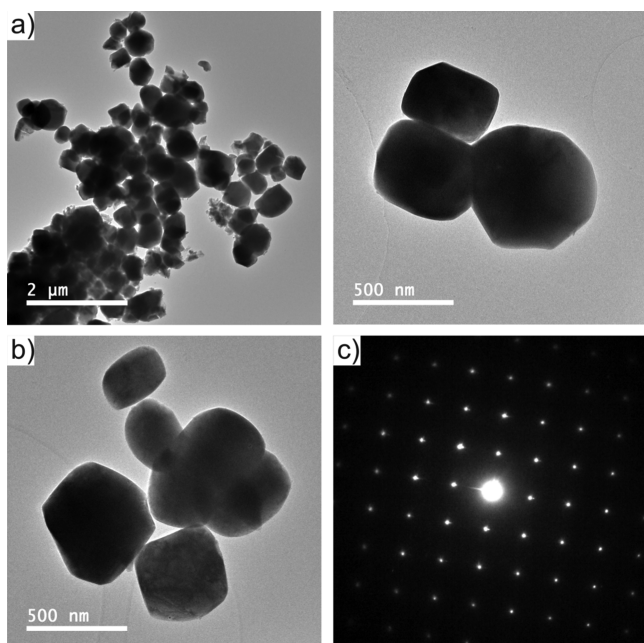
Figure 5. Evolution of the lattice parameters during heating and cooling of 1.2 H CaH$_2$-reduced BaTiO$_3$ in air. Standard deviations are less than the size of the symbols.

parameter of the cubic high-temperature form of BaTiO$_3$ is clearly smaller than that of the reduced samples [by about 0.07 Å for 1.2-H-CaH$_2$ and by about 0.015 Å for 1.2-H-MgH$_2$ (Supporting Information, Figure S1)].

The influence of reaction time is depicted in Figure 6 for the 1.2 H reductions, and results from the refinement of the PXRD

Figure 3. (a) TEM images of the BaTiO$_3$ starting material (with an average particle size of 500 nm according to the specification of the supplier). (b) TEM image of a 1.2 H CaH$_2$-reduced sample. (c) Electron diffraction pattern along [001] shows cubic symmetry.
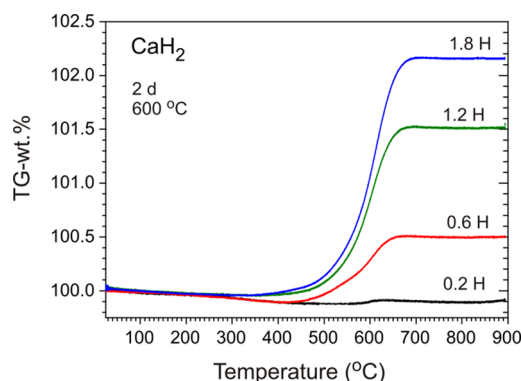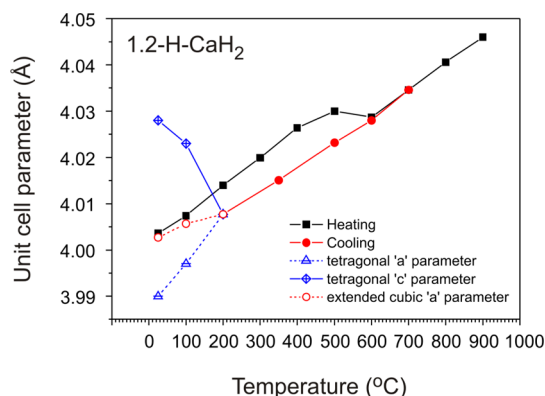

Figure 4. TGA traces for products obtained from the hydride reduction of BaTiO$_3$ at 600 °C during 2 days, using various concentrations of CaH$_2$.

0.6-H-CaH$_2$ up to 450 °C, and for 1.2-H-CaH$_2$ and 1.8-H-CaH$_2$ up to 350 °C. The initial weight loss relates well to the TG behavior of the starting material, which shows a continuous weight loss amounting to 0.15% up to 700 °C (as shown later). The subsequent weight increase should be due to oxidation, which for all samples is completed above 700 °C. The associated x values according to eq 4 are contained in Table 2. The value $x = 0.34$ for the 1.8-H-CaH$_2$ sample is clearly below the maximum value reported by Kobayashi et al. ($x \approx 0.6$).[10,13]

Figure 5 shows the lattice parameter variation as a function of temperature as obtained from a multi-temperature PXRD experiment in which the 1.2-H-CaH$_2$ sample was heated in air to 900 °C and subsequently cooled. In agreement with the TGA experiment, oxidation occurs between 500 and 600 °C. Above 600 °C, the lattice parameters during heating and cooling coincide. Upon cooling, the phase transition into tetragonal BaTiO$_3$ occurs below 200 °C.[23] The lattice

Figure 6. PXRD patterns (a) and TGA traces (b) of products obtained from the hydride reduction of BaTiO$_3$ with 1.2 H CaH$_2$ at 600 °C during 1, 2, 4, and 7 day experiments. The arrow marks a reflection from Ti$_3$O in the 7 day pattern.

data are compiled in Table 3. All products represent mixtures of two cubic phases. The 1- and 2 day experiments produced virtually identical products, which are also very similar to the 4 day experiment, whereas the product of the 7 day experiment is clearly different. The PXRD pattern shows significantly broader reflections and also the presence of an impurity phase (Ti$_3$O), which is indicative of the onset of decom-

Table 3. Synthesis Products from Hydride Reduction with 0.6 M CaH₂ at 600 °C at Varying Reaction Times

1.2-H-CaH₂ reaction time	product/fraction (wt %)	lattice parameters (Å)	volume (Å³)	x from TG
1 d	cubic-I/91(2)	4.0093(2)	64.446(4)	0.24
	cubic-II/9(2)	4.0219(1)	65.056	
2 d	cubic-I/87(2)	4.0079(1)	64.380(4)	0.24
	cubic-II/13(2)	4.0205(1)	64.987	
4 d	cubic-I/89(2)	4.0094(1)	64.451(4)	0.26
	cubic-II/11(2)	4.0221(1)	65.068	
7 d	cubic-I/70(1)	4.0173(1)	64.834(2)	0.51
	cubic-II/28(1)	4.0275(1)	65.330	
	Ti₃O/2(1)			

Table 4. Synthesis Products from Hydride Reduction with NaH, MgH₂, NaBH₄, and NaAlH₄ during 2 Day Experiments at 600 °C

sample	product/fraction (wt %)	lattice parameters (Å)	volume	x from TG[a]
0-H	tetragonal	$a = 3.9964(1)$, $c = 4.0310(1)$	64.379(2)	0
NaH				
0.2-H	tetragonal	$a = 3.9989(1)$, $c = 4.0197(1)$	64.280(3)	N/A
0.6-H	tetragonal	$a = 4.0001(1)$, $c = 4.0171(1)$	64.276(2)	N/A
1.2-H	tetragonal	$a = 4.0002(1)$, $c = 4.0164(1)$	64.269(2)	N/A
1.8-H	tetragonal	$a = 4.0007(1)$, $c = 4.0151(1)$	64.263(3)	N/A
MgH₂				
0.2-H	cubic	4.0046(1)	64.222(1)	0.04
0.6-H	cubic	4.0091(1)	64.438(2)	0.21
1.2-H	cubic	4.0198(1)	64.954(2)	0.41
1.8-H	cubic-I/48(1)	4.0331(1)	64.96(1)	0.55
	cubic-II/52(1)	4.0199(1)	64.566(9)	
NaBH₄				
0.2-H	tetragonal	$a = 4.0017(1)$, $c = 4.0132(1)$	64.265(3)	0.04
0.6-H	cubic	4.0046(1)	64.220(1)	0.18
1.2-H	cubic	4.0046(1)	64.216(2)	0.36
1.8-H	cubic	4.0045(1)	64.217(2)	0.60
NaAlH₄				
0.2-H	cubic	4.0045(1)	64.22(2)	0.05
0.6-H	cubic-I/83(1)	4.0065(1)	64.312(1)	0.19
	cubic-II/17(1)	4.0155(1)	64.747(1)	
1.2-H	cubic-I/44(1)	4.0107(1)	64.514(1)	0.39
	cubic-II/56(1)	4.0202(1)	64.973(1)	
1.8-H	cubic-I/30(3)	4.0220(1)	64.78(1)	0.56
	cubic-II/70(3)	4.0163(3)	65.064(9)	

[a] x refers to a reaction $BaTiO_{3-x}H_x + 0.75xO_2 \rightarrow BaTiO_3 + 0.5xH_2O$.

position of BaTiO₃. The unit cell parameters are increased with respect to the products obtained after shorter times. Peculiar is the TGA trace, exhibiting significant weight loss (~0.4%) between room temperature and 350 °C, after which a weight increase in excess of 3% occurs. We also mention briefly the influence of temperature. Below 550 °C, the reactivity of CaH₂ is low and a conversion into a cubic product was not observed after 5 days. Temperatures above 650 °C represented harsh conditions, equivalent to long reaction times and/or high concentrations of CaH₂, H/BaTiO₃ > 4.

To summarize, we could reproduce the hydride reduction of BaTiO₃ with CaH₂ as reported by Kobayashi et al.[10,13] At the same time, we noticed profound differences, such as heterogeneous products, which indicates that the hydride reduction of BaTiO₃ is sensitive to the experimental conditions.

3.3. Reduction with NaH, MgH₂, NaBH₄, and NaAlH₄. Hydride reduction of BaTiO₃ has hitherto only been reported with CaH₂. In the following, we describe the reaction with the reductants NaH (MH), MgH₂ (MH₂), and NaBH₄ and NaAlH₄ (MH₄). Originally, we also included LiH, LiBH₄, and LiAlH₄ in this investigation. However, Li-containing metal hydrides exhibited a different behavior, which not only involved H but also Li as the reactive species toward the modification of BaTiO₃. A detailed investigation of the Li-containing metal hydride reactions will be reported elsewhere. The decomposition temperatures of NaH, MgH₂, NaBH₄, and NaAlH₄, referring to an equilibrium pressure of 1 bar, are in the range 300−400 °C, which is substantially lower than that of CaH₂ (~600 °C).[24] Consequently, one may expect a substantial H₂ gas-phase contribution to hydride reduction. The results are compiled in Table 4, in Figure 7 (TGA traces), and in the Supporting Information (Figure S2, PXRD patterns).

All samples from NaH reductions displayed a pale blue color, and the PXRD patterns (Figure S2a) show that conversion to a cubic product was not achieved. The trend in the lattice parameters indicates decreased tetragonality with increasing NaH concentration (Table 4). The TGA traces (Figure 7a) reveal a small weight loss up to 350 °C (0.25−0.45%), which is followed by a slightly irregular behavior up to 700 °C, above which weights are constant. In Figure 7a included is the TG trace of the starting material. BaTiO₃ exhibited a small (0.15%) weight loss between room temperature and 740 °C. The continuous nature of this weight loss indicates gradual release of water, initially physically adsorbed water on surface hydroxyls and then water from the condensation of surface hydroxyls. Typically, surface hydroxyls

have various bonding energies and are desorbed over a wide temperature range.[25,26] We infer that this small weight loss is also present in metal hydride-reduced samples. During TGA, this process overlaps with the weight increase because of oxidation, thus leading to a minor underestimation of the weight increase. The weight loss of the NaH-reduced samples significantly exceeds that of the starting material. This suggests that reduction primarily affected and modified the surface of BaTiO₃ particles, which, after washing, resulted in a higher concentration of hydroxyl and absorbed water. Note that the TGA weight loss behavior (up to 350 °C) of the NaH-reduced samples and the 1.2-H-CaH₂-7d sample appears to be very similar (cf. Figure 6b).

Using MgH₂ as the reducing agent yielded the cubic phase already with 0.2 H (Figure S2b). The samples produced with 0.2 H, 0.6 H, and 1.2 H represented single-phase products, with the lattice parameter increasing from 4.005 to 4.020 Å (Table 4). With 1.8 H, a mixture of two phases—with lattice parameters 4.020 and 4.033 Å and roughly equal proportions—was obtained. Generally, the lattice parameters of the MgH₂-reduced samples are larger compared to that of the CaH₂-reduced ones. Also, and perhaps related, the TGA weight increase (Figure 7b) due to oxidation is larger compared to that of CaH₂-reduced ones. The x value attained for the 1.8-H-MgH₂ sample approaches the maximum value 0.6 proposed by Kobayashi et al.[10] The results for NaAlH₄ are
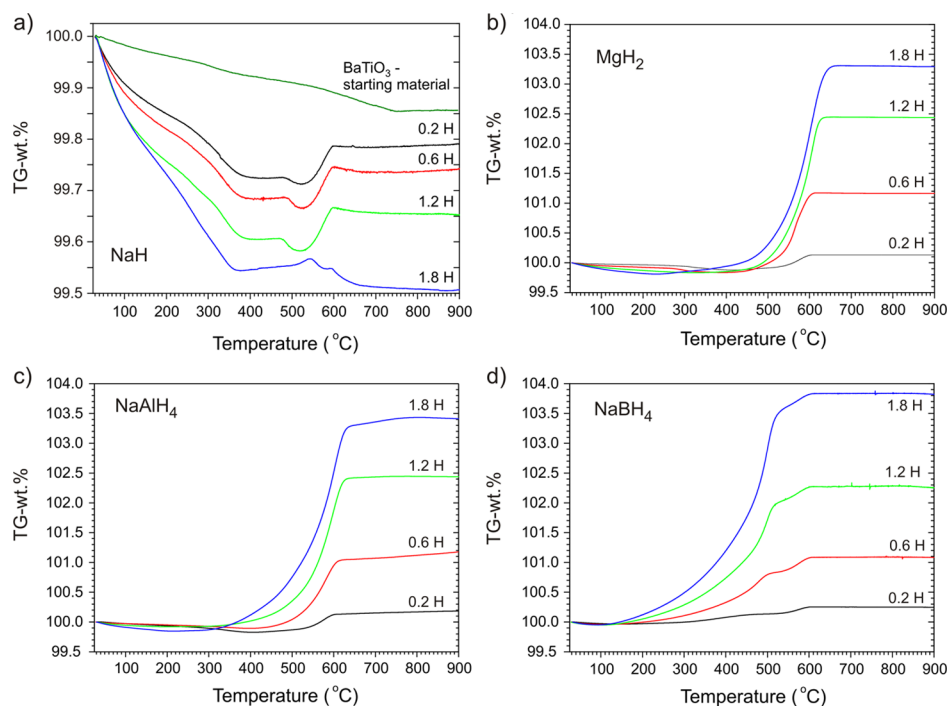
Figure 7. TGA traces of products obtained from the hydride reduction of BaTiO$_3$ at 600 °C during 2 day experiments using NaH (a), MgH$_2$ (b), NaAlH$_4$ (c), and NaBH$_4$ (d). (a) also contains the TGA trace of the starting material.

shown in Figures 7c and S2c. Similar to MgH$_2$ reduction, a single-phase cubic product is obtained already with 0.2 H. The samples 0.6-H-NaAlH$_4$, 1.2-H-NaAlH$_4$, and 1.8-H-NaAlH$_4$, however, represented two phase mixtures. The TGA traces of NaAlH$_4$- and MgH$_2$-reduced samples compare well.

The results for the NaBH$_4$ reductions are shown in Figures 7d and S2d. The sample 0.2-H-NaBH$_4$ corresponded to the tetragonal phase, whereas higher synthesis H concentrations afforded single-phase cubic products. Remarkably, the lattice parameter of these products shows virtually no dependence on synthesis H concentration and attains a comparatively small value, 4.005 Å (Table 4). The TGA traces of the NaBH$_4$-reduced samples (Figure 7d) are different from those of the CaH$_2$-, MgH$_2$-, and NaAlH$_4$-reduced ones, in that the weight increase is already observed between 200 and 400 °C, that is, at temperatures about 200 °C lower. In addition, a peculiar kink near 500 °C is noticeable, which suggests that the oxidation occurs in two steps. Above 650 °C, the weights are constant and the total weight increases compare well with the corresponding MgH$_2$- and NaAlH$_4$-reduced samples.

In summary, NaH acts only as a weak reducing agent toward BaTiO$_3$, which should relate to the low decomposition temperature of NaH, possibly making gaseous H$_2$ the reducing species. We conjecture that reduction with NaH primarily affects and modifies the surface of BaTiO$_3$ particles. The other metal hydrides afford cubic products. The TGA weight increase for NaBH$_4$-, MgH$_2$-, and NaAlH$_4$-reduced samples is very similar, with x values for 1.8 H products being near to 0.6, which was previously reported as the maximum value for BaTiO$_{3-x}$H$_x$.[10] Judging from the TGA weight increase (x values) of the reduced samples, the reductive reactivity of CaH$_2$ appears to be lower compared to that of MgH$_2$, NaAlH$_4$, and NaBH$_4$. From the PXRD, one can notice differences between the cubic products obtained with the various reductants. Products from NaBH$_4$ reduction are distinguished

in that they are single phase even at the highest H concentrations applied, whereas the other reductants yield mixtures of two cubic phases with increasing H concentration. MgH$_2$-reduced samples attain the largest lattice parameters. With respect to unit cell parameters, one may discern three main scenarios, 4.005 Å—NaBH$_4$, 4.01 Å—CaH$_2$, and 4.02 Å—MgH$_2$. We note that 0.1 HAc as the washing agent removed effectively the oxides MgO and "NaAlO$_2$", which is rather difficult when using NH$_4$Cl/MeOH. Using NaBH$_4$ as the reducing agent yielded an amorphous side product that could not be removed by washing with a weak acid. The presence of amorphous "NaBO$_2$" only became apparent when analyzing the samples after TGA. The PXRD pattern showed extra reflections from BaTi(BO$_3$)$_2$, presumably formed according to 2 NaBO$_2$ + BaTiO$_3$ → BaTi(BO$_3$)$_2$ + Na$_2$O. Perhaps this reaction also influences the shape of the TG curve and may explain the peculiar kink feature near 500 °C.

3.4. Solid-State ^{1}H MAS NMR Investigations. ^{1}H MAS NMR has not yet been considered for the detailed analysis of new BaTiO$_{3-x}$H$_x$. Kobayashi et al., in their initially report on BaTiO$_{3-x}$H$_x$, showed a spectrum with a single sharp signal at 4.4 ppm (the sample composition was not stated).[10] They concluded that all H species are in the same chemical state and environment, in agreement with a defect-free solid solution in which O^{2-} is randomly replaced by H$^-$ in the perovskite structure.

Figure 8 shows ^{1}H MAS NMR spectra recorded of the starting material before and after TGA, that is, before and after heating to 900 °C in air. Three distinct resonances are observed at 1.1, 4.8, and 6.5 ppm, together with two shoulders at ~2 and ~4 ppm, respectively. All of these proton signals are attributed to the surface OH species; the presence of structural hydroxyl in the starting material is excluded because of the great similarity of the spectra before and after TGA. Unlike surface OH, structural OH will not reform upon exposure to
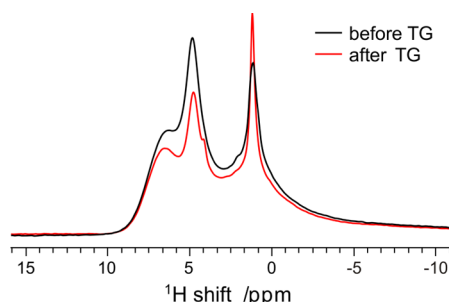
Figure 8. ^{1}H MAS NMR spectrum of the BaTiO$_3$ starting material before (black line) and after (red line) heating to 900 °C in air flow (during a TGA experiment).

Figure 9. (a) ^{1}H MAS NMR spectra of 0.2 and 1.2 H CaH$_2$-reduced samples (600 °C, 2 day synthesis). (b) ^{2}H MAS NMR spectrum of a 1.2 D CaD$_2$-reduced sample (600 °C, 2 day synthesis). The dotted line highlights the identical location of the maxima of the broad resonances in the ^{1}H and ^{2}H spectra. (c) Close-up of the resonances in the positive parts per million range. The inset shows integrated proton signal intensity with respect to the starting material (BaTiO$_3$). The signal of the 1.2-H sample is deconvoluted into a protic (positive parts per million) and hydridic (negative parts per million) contribution.

ambient atmosphere after the TGA treatment. Also, the occurrence of structural OH is more typical for the hydrothermally synthesized BaTiO$_3$, which are afforded as nanoparticles with cubic symmetry.[25−28] These are clearly not the characteristics of our starting material (cf. Figure 3a). Because the distinct chemical shifts of ^{1}H resonances stem from the specific surface environments, the bonding energies associated with the respective proton sites are also likely to differ, which is reflected by the continuous weight loss seen in the TG experiment (cf. Figure 7a).

Figure 9a shows the ^{1}H MAS NMR spectra recorded from the 0.2-H-CaH$_2$ and 1.2-H-CaH$_2$ samples. The most noticeable difference is a broad resonance centered at −18 ppm, with an additional shoulder at −60 ppm, which appears in the spectrum of the 1.2-H-CaH$_2$ sample and which is absent in the spectrum of 0.2-H-CaH$_2$. We attribute this signal to hydridic H on the O position in the perovskite structure. This is unambiguously corroborated by the ^{2}H MAS NMR spectrum of the analogous sample 1.2-D-CaD$_2$, which was prepared in the same way as the 1.2-H-CaH$_2$ specimen (i.e., 2 day synthesis at 600 °C), but with a deuterated reducing agent. Obviously, the hydroxyl resonances are absent in the ^{2}H spectrum, which shows a single signal that exhibits the same chemical shift as the broad resonance in the ^{1}H spectrum (Figure 9b). The ^{1}H MAS NMR signals of 0.2-H-CaH$_2$ and 1.2-H-CaH$_2$ in the (positive) 0−10 ppm range have a similar pattern (seen in Figure 9c). When compared to the untreated BaTiO$_3$, the CaH$_2$-reduced samples exhibit additional signals in the 1−7 ppm region and also altered intensities. This indicates that upon reduction (and subsequent washing), additional surface OH sites are created, along with a population redistribution of the pre-existing ones.

As a next step, we attempted to quantify the H content of the BaTiO$_3$ starting material by relating its ^{1}H NMR signal intensity to that of adamantane (C$_{10}$H$_{16}$) in the same rotor volume and under identical experimental conditions. The BaTiO$_3$ sample (before TGA) exhibits a total ^{1}H NMR signal integral of 0.94% compared to the adamantane sample. From the densities and molecular weights of adamantane (1.08 g/cm^3, 136.23 g/mol) and BaTiO$_3$ (6.02 g/cm^3, 233.2 g/mol), a molar ratio of H/BaTiO$_3$ ≈ 0.039 can then be derived. This ratio relates well to the TGA weight loss of the BaTiO$_3$ starting material (0.15%, cf. Figure 7b): when attributing this weight loss to H$_2$O, one obtains a molar ratio H$_2$O/BaTiO$_3$ ≈ 0.02 (i.e., H/BaTiO$_3$ = 0.04). In order to quantify the H content of the reduced samples, we related their ^{1}H NMR signal integrals to this value. This is demonstrated in the inset of Figure 9c. In addition, the ^{1}H signals can be deconvoluted into a protic
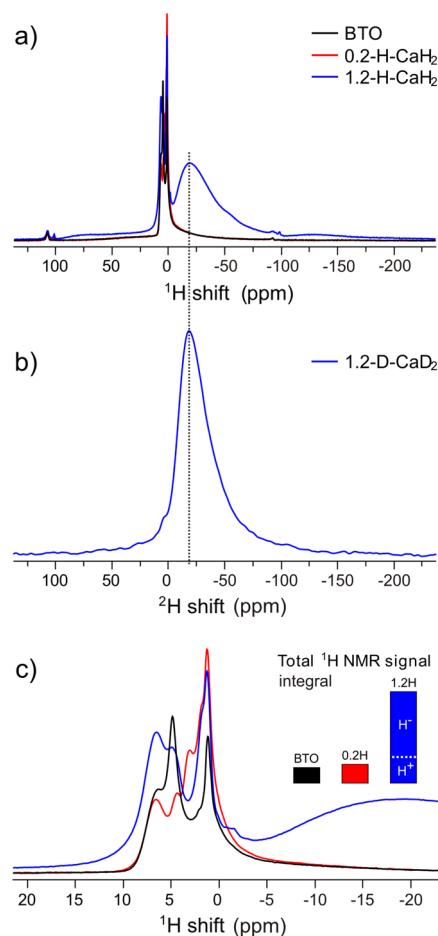
(positive parts per million) and hydridic (negative parts per million) part.

Surprisingly, the total ^{1}H NMR signal integral for 1.2-H-CaH$_2$ is only approximately 5 times larger than that of the 0.2-H-CaH$_2$ sample (which in turn is only slightly higher than that of the starting material). From deconvolution of the total ^{1}H NMR signal integral for 1.2-H-CaH$_2$, one can estimate the molar ratio between hydridic H and BaTiO$_3$ to be approximately 0.16. The large discrepancy with the TGA experiment (cf. Figure 4), which delivers an x value of 0.24 with respect to BaTiO$_{3−x}$H$_x$, has to be attributed to the simultaneous presence of O vacancies. As a matter of fact, the combined ^{1}H MAS NMR and TGA results suggest that hydridic H and O vacancies are present in roughly equal concentrations. Thus, we reformulate 1.2-H-CaH$_2$ as BaTiO$_{3−x}$H$_y$□$_{(x−y)}$ with x ≈ 0.24 and y ≈ 0.16 and conclude that ^{1}H MAS NMR spectroscopy represents a reliable and convenient method to analyze H environments and assess H contents in reduced BaTiO$_3$ samples.

The observed negative shift for the hydridic ^1H can be attributed to the contact hyperfine interaction between the 3d electrons of Ti(III) and the ^1H nucleus. This shift mechanism is operative in both metallic systems and paramagnetic insulators.[29,30] In metallic systems, the electrons are delocalized in a conduction band and the hyperfine interaction results in a Knight shift that depends on the density of states at the Fermi level.[31] The magnitude of the Knight shift is known to increase with both the unit cell volume[32] and the concentration of charge carriers.[33] In paramagnetic insulators, the shift mechanism is dominated by the Fermi-contact hyperfine interaction of ^1H with the 3d electron of the directly bonded Ti(III) ion, which gives a Fermi-contact shift.[29] In the latter case, the electronic conductivity is hypothesized to arise from the electron polaron formation between localized states formed in the band gap. Both mechanisms may give negative shifts, if the hyperfine interaction is dominated by a spin polarization mechanism. The identity of the shift mechanism in our reduced $BaTiO_3$ samples is addressed in the following discussion.

The ^1H MAS NMR spectra recorded from the series of 0.2 H-reduced samples are shown in Figure 10. Although surface
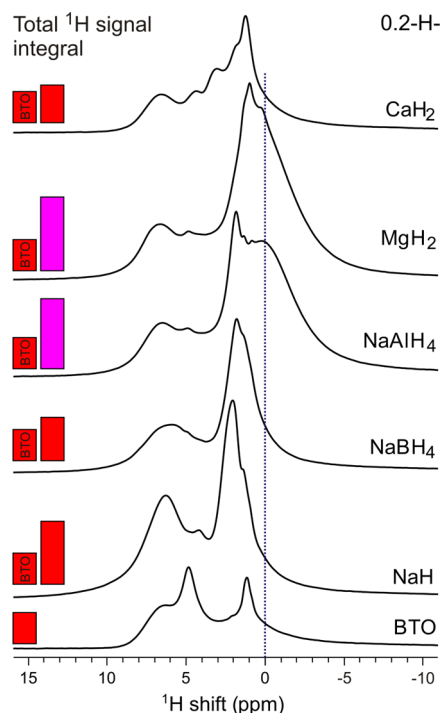

Figure 10. ^1H MAS NMR spectra of the 0.2-H sample series. The blue dotted line indicates an additional resonance in the 0.2-H-MgH_2 and 0.2-H-$NaAlH_4$ spectra at ~0 ppm, which is attributed to hydridic H. The inset shows integrated ^1H signal intensity with respect to the starting material ($BaTiO_3$). The violet color for 0.2-H-MgH_2 and 0.2-H-$NaAlH_4$ illustrates a mixture of protic and hydridic H.

hydroxyl sites and their respective populations are altered, one recognizes a general similarity with the starting material. More interestingly, the spectra of 0.2-H-MgH_2 and 0.2-H-$NaAlH_4$ specimens have an additional resonance at around 0 ppm. As discussed previously, these samples are cubic, whereas the other 0.2 H-reduced materials remained tetragonal. We therefore interpret this additional resonance at around 0 ppm as being from hydridic H. The total ^1H signal of the 0.2-

H-CaH_2 and 0.2-H-$NaBH_4$ samples is similar to that of the starting material (H/$BaTiO_3$ ≈ 0.04), whereas that of the remaining samples is by 70−80% higher. For 0.2-H-NaH, this is clearly due to an increased concentration of surface OH. For 0.2-H-MgH_2 and 0.2-H-$NaAlH_4$, the higher ^1H concentration is attributed to the hydridic contribution. This contribution, y, can then be estimated to be ~0.03, which is slightly lower than the x values obtained from TGA, 0.04−0.05 (cf. Table 4). The relatively small hydride shifts observed for 0.2-H-MgH_2 and 0.2-H-$NaAlH_4$ compared to 1.2-H-CaH_2 may then be consistent with a Knight shift for all the three samples: 1.2-H-CaH_2 has a considerably higher concentration of hydride and also vacancies and therefore a higher concentration of charge carriers, which in turn results in a more negative Knight shift.

Figure 11 shows the ^1H MAS NMR spectra recorded for the series of 1.2 H-reduced samples. First, 1.2-H-NaH, which is tetragonal, does not exhibit a hydridic component, as expected given the results discussed previously. However, the spectrum does reveal a high concentration of surface hydroxyl, with an especially intense resonance at around 1 ppm. This supports the conjecture that reduction with NaH primarily affects the surface of the particles: that is, reduction leads to a high concentration of vacancies at the surface, which subsequently terminate/react into hydroxyl during the washing process. The spectrum of 1.2-H-$NaBH_4$ has a distinct signal with a small negative shift of −1.8 ppm, which is assigned to hydridic H. Note that the comparatively low shift is similar to that observed for 0.2-H-MgH_2 and 0.2-H-$NaAlH_4$. As already discussed, 1.2-H-CaH_2 exhibits a broad resonance with a maximum at around −18 ppm and with a shoulder at around −60 ppm. The ^1H NMR signals at negative shifts for the 1.2-H-$NaAlH_4$ and 1.2-H-MgH_2 samples are even broader with their peak maxima at around −30 and −60 ppm, respectively. Clearly, among the 1.2-H reduced samples, 1.2-H-$NaBH_4$ is distinguished because of its relatively sharp ^1H MAS signal, which indicates a homogeneous coordination environment for H, and low shift. As will be discussed in the next section, this sample contains a low concentration of hydride, y ≈ 0.04, which is comparable to that of 0.2-H-MgH_2 and 0.2-H-$NaAlH_4$.

We now remark on a possible correlation between the shifts and line widths of the hydridic ^1H resonances, which broaden according to $NaBH_4$ < CaH_2 < $NaAlH_4$ < MgH_2 and concurrently shift toward more negative parts per million values. The shoulder at −60 ppm in the spectrum for 1.2-H-CaH_2 and a pronounced asymmetry of the negative parts per million signal in the spectrum for 1.2-H-$NaAlH_4$ probably relate to the two-phase nature of these samples. We recall that both samples constituted two cubic phases with lattice parameters ~4.01 and ~4.02 Å and one is tempted to correlate the shift to the size of the lattice parameter: 4.005 Å—−2 ppm ($NaBH_4$, single phase); 4.01 Å—−20 to −30 ppm (CaH_2, $NaAlH_4$, two-phase); 4.02 Å—−60 ppm (MgH_2, single phase). This is corroborated by the ^1H MAS NMR spectra from the samples obtained by 1.2 H CaH_2 reduction during 1, 2, 4, and 7 days (Supporting Information, Figure S3). The similarity of the 1, 2, and 4 day samples established from PXRD and TGA (cf. Figure 6) is also reflected in their virtually identical ^1H MAS NMR responses. The spectrum of the 7 day sample, however, reveals a largely asymmetric resonance with the peak maximum at around −50 ppm. Concomitant with the more negative shift of the NMR signal of hydridic H is an
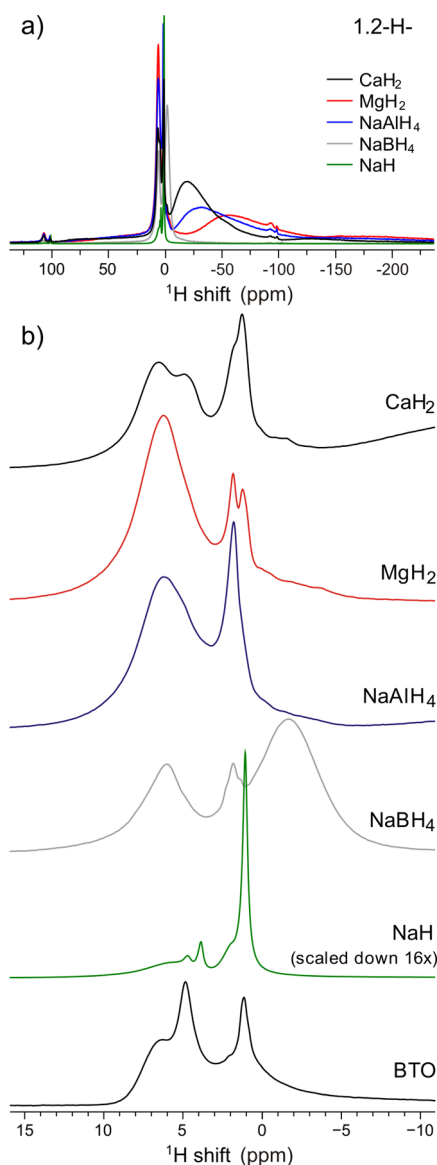
Figure 11. (a) ^{1}H MAS NMR spectra of the 1.2-H sample series. (b) Close-up of the resonances in the positive parts per million range attributed to protic (surface) H species. Note that the close-up also contains the signal from hydridic H for 1.2-H-NaBH$_4$, which is centered at −1.8 ppm.

increase of the lattice parameter of the majority phase from ~4.01 to ~4.02 Å (cf. Table 3).

This gradual shifting of the resonance to more negative shifts is consistent with the behavior previously observed for metallic hydrides such as NbH$_x$, where an increase in the magnitude of the Knight shift correlates with an increasing unit cell volume.[32] This observation suggests that our reduced 1.2-H samples correspond to metals with delocalized electrons in a conduction band, as opposed to electron polaron formation, leading to localized states in the band gap. Thus, the observed ^{1}H shifts are Knight shifts. Values are consistent with the ranges observed for other metallic hydride materials, which are typically 0 to −250 ppm.[34] As mentioned above, the magnitude of the Knight shift also depends on the density of states at the Fermi level.[31] This in turn should correlate with the charge carrier concentration, and one would also expect that the charge carrier concentration in our samples increases

with increasing Knight shift. However, the overall trends are complicated to predict. Kageyama et al. reported measurable electrical conductivities for their materials BaTiO$_{2.4}$H$_{0.6}$ and BaTiO$_{2.7}$H$_{0.3}$, while at the same time their ^{1}H MAS NMR spectrum indicates the absence of the Knight effect.[10] This may be explained by assuming a different electronic structure and conduction mechanism, that is, thermally activated polaron hopping. However, we note that the ^{1}H MAS NMR spectrum reported by Kageyama et al. showing a single sharp resonance at 4.4 ppm is slightly inconceivable because a more complex spectrum is expected from the simultaneous presence of unavoidable surface hydroxyl and surface water.

3.5. Oxyhydride versus O Vacancy Formation. It appears that the hydride reduction of BaTiO$_3$ is strongly influenced by the reducing agent (metal hydride) and that reduced BaTiO$_3$ actually represents complex heterogeneous materials because of the simultaneous presence of vacancies and H in the anion substructure. The overall concentration of hydridic H is comparatively rather low.

Figure 12 presents the results of the ^{1}H MAS NMR spectral deconvolution into positive(protic)- and negative(hydridic)-
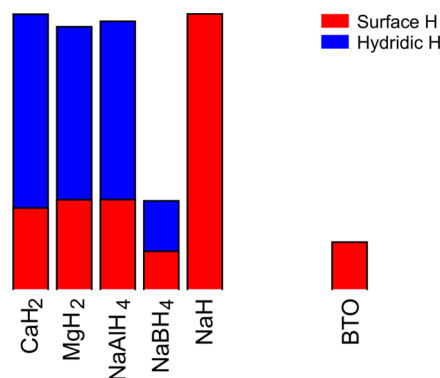

Figure 12. Relative strengths and shift contributions to the ^{1}H MAS NMR signal integral of the 1.2-H series of reduced BaTiO$_3$ samples.

parts per million shift contributions to the total proton signal of 1.2 H-reduced BaTiO$_3$ samples. It is seen that 1.2-H-MgH$_2$ and 1.2-H-NaAlH$_4$ have a very similar hydridic H content as 1.2-H-CaH$_2$. Surprising is the high H content of the 1.2-H-NaH sample, which, however, refers to protic (surface) hydroxyl, and the low hydridic H content (on the order of 0.04) of 1.2-H-NaBH$_4$. This implies that O vacancies dominate in the NaBH$_4$-reduced sample. Thus, when using the formula BaTiO$_{3−x}$H$_y$□$_{(x−y)}$ for hydride-reduced BaTiO$_3$, x as estimated from TGA is ~0.35 (cf. Table 4) and y is ~0.04. Accordingly, the H$^-$/O vacancy ratio is around 1:10. Analogous reasoning for the MgH$_2$- and NaAlH$_4$-reduced samples yields y values similar to the CaH$_2$-reduced sample (0.14−0.15); however, because of the significantly larger x (around 0.4), O vacancy concentrations for these samples exceed the concentration of hydridic H by 2−3 times. The compositions of 1.2-H samples derived from the combined TGA and NMR analysis are compiled in Table 5.

The formation of O-deficient phases BaTiO$_{3−x}$H$_y$□$_{(x−y)}$ is surprising and at variance with the results of Kobayashi et al.[10,13] The question arises whether these phases represent intermediates toward stoichiometric oxyhydride formation. Bridge et al. pointed out the significance of gaseous H$_2$ present in the hydride reduction of LaSrCo$_3$O$_4$ for obtaining LaSrCo$_3$H$_{0.7}$.[18] In addition, perhaps Kobayashi et al. attained

Table 5. Compositions of 1.2-H Samples from Hydride Reductions during 2 Days at 600 °C

sample	x_H from TG[a]	$x_\square$ from TG[b]	y from NMR	formula $BaTiO_{3-x}H_{yx-y}$
CaH$_2$	0.24	0.23	0.16	$BaTiO_{3.76}H_{0.16}\square_{0.08}$
MgH$_2$	0.41	0.39	0.14	$BaTiO_{3.60}H_{0.14}\square_{0.26}$
NaAlH$_4$	0.39	0.37	0.15	$BaTiO_{3.62}H_{0.15}\square_{0.23}$
NaBH$_4$	0.36	0.34	0.04	$BaTiO_{3.65}H_{0.04}\square_{0.31}$

[a]x_H refers to a reaction $BaTiO_{3-x}H_x + 0.75xO_2 \rightarrow BaTiO_3 + 0.5xH_2O$. [b]$x_\square$ refers to a reaction $BaTiO_{3-x} + 0.5xO_2 \rightarrow BaTiO_3$.

during their synthesis of $BaTiO_{3-x}H_x$—for unknown reasons—a pressurized H$_2$ atmosphere. Following this conjecture, we subjected the CaH$_2$-, MgH$_2$-, and NaAlH$_4$-reduced samples to pressurized H$_2$ atmospheres (30−50 bar) at 600 °C, which is the temperature applied in the preceding hydride reduction. The results are summarized in Table S1 (Supporting Information) and Figure 13. Interestingly, during annealing
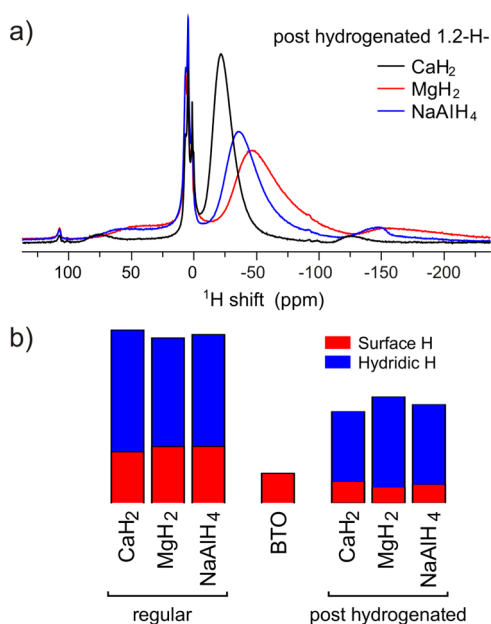

Figure 13. (a) ^1H MAS NMR spectra of posthydrogenated samples. (b) Comparison of relative strengths and shift contributions to the ^1H MAS NMR signal integral for regular and posthydrogenated 1.2-H samples.

under pressurized H$_2$, the two-phase samples essentially became single phase, with a lattice parameter closely corresponding to the previous majority phase (Table S1, cf. Table 2). The ^1H NMR spectra (Figure 13) revealed that the annealing procedure did not lead to an increased hydride content. However, the signal narrowed significantly, which indicates that more ordered phases $BaTiO_{3-x}H_y\square_{(x-y)}$ were obtained (cf. Figure 11a and Supporting Information, part V, where spectra of post- and prehydrogenated samples are directly compared). Apparent again is a correlation of the size of the lattice parameter and the chemical shift of the ^1H resonance: the larger the parameter, the more negative the shift is. The TGA weight increases are by about 20% lower after the annealing procedure. This coincides with a lower H content of the posthydrogenated samples. The diminished hydridic H content may be due to a slight oxidation of the sample from traces of oxygen in the autoclave setup.

In summary, it remains unclear why our hydride reduction experiments with BaTiO$_3$ resulted in a different product as described by Kobayashi et al. Yet, highly O-deficient $BaTiO_{3-x}H_y\square_{(x-y)}$ is an interesting material. Reduced $BaTiO_{3-x}$, with applications in electroceramics, electrocatalysis, and electronics, has been described and studied earlier.[35] There is general agreement that the crystal symmetry changes from tetragonal to cubic for small values of x, $x < 0.02$, before transforming to the hexagonal 6H-perovskite for $x > 0.02$.[36,37] The hexagonal form can maintain a maximum x of about 0.15.[38] Characteristic for all forms O-deficient $BaTiO_{3-x}$ is their blue/black color. Cubic $BaTiO_{3-x}$ is synthesized at temperatures 900−1250 °C in a flowing mixture of 5% H$_2$/95% N$_2$. Reduction at higher temperatures results in the hexagonal form.[37] Mixtures of tetragonal and cubic $BaTiO_{3-x}$ are also obtained when sintering BaTiO$_3$ in the reducing environment of an SPS apparatus at 1200 °C,[39,40] and the hexagonal form can be synthesized when heating tetragonal BaTiO$_3$ in a graphite-vacuum furnace to 1300−1500 °C.[38] Against this background, the existence of cubic phases $BaTiO_{3-x}H_y\square_{(x-y)}$ with x values exceeding 0.5 is surprising. Clearly, the incorporation of H plays an important role in stabilizing these highly O-deficient variants of BaTiO$_3$, which in contrast to previously reported forms are accessible at comparatively low temperatures (∼600 °C). The two-phase behavior observed for most reductions may correlate with a segregation of $BaTiO_{3-x}H_y\square_{(x-y)}$ into a vacancy and hydride-rich composition. Interestingly, our defect samples show a similar reactivity toward the formation of mixed-anion derivatives as that reported for $BaTiO_{2.5}H_{0.5}$.[12] For example, $BaTiO_{3-x}H_y\square_{(x-y)}$ can be easily converted into green-colored nitridized BaTiO$_3$ ($BaTiO_{3-\delta}N_y$) under a stream of N$_2$ gas at temperatures above 450 °C.

4. CONCLUSIONS

Following previous reports on the reaction of tetragonal BaTiO$_3$ with CaH$_2$ yielding cubic oxyhydrides $BaTiO_{3-x}H_x$,[10,13] we investigated hydride reduction of BaTiO$_3$ with various metal hydrides as reducing agents. At the applied temperature of 600 °C, we find that NaH acts only as a weak reducing agent. A conversion into a cubic product is not obtained. This is attributed to the low decomposition temperature of NaH, instead of making H$^-$ gaseous H$_2$ the reducing species. Apart from the originally employed CaH$_2$, also MgH$_2$ and the ternary hydrides NaBH$_4$ and NaAlH$_4$ reduce BaTiO$_3$ to a blue-/black-colored cubic product. However, at variance with the original reports, we find that only a small concentration of H replaces O in the anionic substructure of BaTiO$_3$. Instead, highly O-deficient disordered cubic phases $BaTiO_{3-x}H_y\square_{(x-y)}$ with x up to 0.6 and y in a range 0.04−0.25 are obtained. The existence of such phases is surprising, and the incorporation of H supposedly plays an important role in stabilizing these highly O-deficient variants of BaTiO$_3$. These defective samples show high reactivity toward the formation of mixed-anion derivatives, such as oxynitrides. Finally, we emphasize the important role of NMR spectroscopy for characterizing both H species and H contents in reduced BaTiO$_3$ samples. The negative shift of hydridic H is attributed to the metallic nature of the phases $BaTiO_{3-x}H_y\square_{(x-y)}$.

■ ASSOCIATED CONTENT

ⓢ Supporting Information

The Supporting Information is available free of charge on the ACS Publications website at DOI: 10.1021/acsomega.8b01368.

Evolution of the lattice parameters during heating and cooling of 1.2 H MgH_2-reduced $BaTiO_3$ in air; PXRD patterns of products obtained from the hydride reduction of $BaTiO_3$ at 600 °C during 2 day experiments using NaH, MgH_2, $NaAlH_4$, and $NaBH_4$; ^1H MAS NMR spectra of products obtained from reduction with 1.2 H CaH_2 at 600 °C during 1, 2, 4, and 7 day experiments; characteristics of products from hydrogenating various reduced samples at 30−50 bar for 24 h at 600 °C; refinement details and Rietveld plots for the products from NaH, CaH_2, CaD_2, MgH_2, $NaAlH_4$, and $NaBH_4$ reductions; details on the study of the effect of different washing agents (0.1 M NH_4Cl/MeOH, 0.1 M HAc, 0.1 M HCl) on a 1.2-H-CaH_2 (600 °C, 2 day synthesis) reference sample; details of the oxidation study of samples 1.2-H-CaH_2 and 1.2-H-MgH_2 in air by in situ PXRD; and details on the analysis of products from annealing in a pressurized (30−40 bar) H_2 atmosphere for 24 h at 600 °C (PDF)

■ AUTHOR INFORMATION

Corresponding Author

*E-mail: Ulrich.Haussermann@mmk.su.se (U.H.).

ORCID ⓞ

Diana Bernin: 0000-0002-9611-2263

Maths Karlsson: 0000-0002-2914-6332

Cheuk-Wai Tai: 0000-0001-7286-1211

Andrew J. Pell: 0000-0002-2542-8113

Ulrich Häussermann: 0000-0003-2001-4410

Notes

The authors declare no competing financial interest.

■ ACKNOWLEDGMENTS

■ REFERENCES

(1) Yamamoto, T.; Kageyama, H. Hydride reductions of transition metal oxides. *Chem. Lett.* **2013**, *42*, 946−953.

(2) Hayward, M. A. Topochemical reactions of layered transition-metal oxides. *Semicond. Sci. Technol.* **2014**, *29*, 064010.

(3) Hadermann, J.; Abakumov, A. M.; Adkin, J. J.; Hayward, M. A. Topotactic Reduction As a Route to New Close-Packed Anion Deficient Perovskites: Structure and Magnetism of 4H-BaMnO2+x. *J. Am. Chem. Soc.* **2009**, *131*, 10598−10604.

(4) Kitchen, H. J.; Saratovsky, I.; Hayward, M. A. Topotactic reduction as a synthetic route for the preparation of low-dimensional Mn(II) oxide phases: The structure and magnetism of LaAMnO4-x (A = Sr, Ba). *Dalton Trans.* **2010**, *39*, 6098−6105.

(5) Hayward, M. A.; Green, M. A.; Rosseinsky, M. J.; Sloan, J. Sodium Hydride as a Powerful Reducing Agent for Topotactic Oxide Deintercalation: Synthesis and Characterization of the Nickel(I) Oxide LaNiO2. *J. Am. Chem. Soc.* **1999**, *121*, 8843−8854.

(6) Tsujimoto, Y.; Tassel, C.; Hayashi, N.; Watanabe, T.; Kageyama, H.; Yoshimura, K.; Takano, M.; Ceretti, M.; Ritter, C.; Paulus, W. Infinite-layer iron oxide with a square-planar coordination. *Nature* **2007**, *450*, 1062−1065.

(7) Seddon, J.; Suard, E.; Hayward, M. A. Topotactic Reduction of YBaCo2O5 and LaBaCo2O5: Square-Planar Co(I) in an Extended Oxide. *J. Am. Chem. Soc.* **2010**, *132*, 2802−2810.

(8) Hayward, M. A.; Cussen, E. J.; Claridge, J. B.; Bieringer, M.; Rosseinsky, M. J.; Kiely, C. J.; Blundell, S. J.; Marshall, I. M.; Pratt, F. L. The Hydride Anion in an Extended Transition Metal Oxide Array: LaSrCoO3H0.7. *Science* **2002**, *295*, 1882−1884.

(9) Poeppelmeier, K. SOLID STATE CHEMISTRY: A Mixed Oxide-Hydride Perovskite. *Science* **2002**, *295*, 1849.

(10) Kobayashi, Y.; et al. An oxyhydride of BaTiO3 exhibiting hydride exchange and electronic conductivity. *Nat. Mater.* **2012**, *11*, 507−511.

(11) Yajima, T.; et al. A labile hydride strategy for the synthesis of heavily nitridized BaTiO3. *Nat. Chem.* **2015**, *7*, 1017−1023.

(12) Masuda, N.; et al. Hydride in BaTiO2.5H0.5: A Labile Ligand in Solid State Chemistry. *J. Am. Chem. Soc.* **2015**, *137*, 15315−15321.

(13) Sakaguchi, T.; et al. Oxyhydrides of (Ca,Sr,Ba)TiO3 Perovskite Solid Solutions. *Inorg. Chem.* **2012**, *51*, 11371−11376.

(14) Yamamoto, T.; et al. An Antiferro-to-Ferromagnetic Transition in EuTiO3-xHx Induced by Hydride Substitution. *Inorg. Chem.* **2015**, *54*, 1501−1507.

(15) Romero, F. D.; Leach, A.; Möller, J. S.; Foronda, F.; Blundell, S. J.; Hayward, M. A. Strontium vanadium oxide-hydrides: "square-planar" two-electron phases. *Angew. Chem., Int. Ed.* **2014**, *53*, 7556−7559.

(16) Kobayashi, Y.; et al. Gas phase contributions to topochemical hydride reduction reactions. *J. Solid State Chem.* **2013**, *207*, 190−193.

(17) Hernden, B. C.; Lussier, J. A.; Bieringer, M. Topotactic Solid-State Metal Hydride Reductions of Sr2MnO4. *Inorg. Chem.* **2015**, *54*, 4249−4256.

(18) Bridges, C. A.; Darling, G. R.; Hayward, M. A.; Rosseinsky, M. J. Electronic Structure, Magnetic Ordering, and Formation Pathway of the Transition Metal Oxide Hydride LaSrCoO3H0.7. *J. Am. Chem. Soc.* **2005**, *127*, 5996−6011.

(19) Rodríguez-Carvajal, J. FULLPROF: A Program for Rietveld Refinement and Pattern Matching Analysis. *Abstracts of the Satellite Meeting on Powder Diffraction of the XV IUCr Congress*, 1990.

(20) Hwang, T.-L.; van Zijl, P. C. M.; Garwood, M. Fast Broadband Inversion by Adiabatic Pulses. *J. Magn. Reson.* **1998**, *133*, 200−203.

(21) Kervern, G.; Pintacuda, G.; Emsley, L. Fast Adiabatic Pulses for Solid-State NMR of Paramagnetic Systems. *Chem. Phys. Lett.* **2007**, *435*, 157−162.

(22) Pell, A. J.; Pintacuda, G. Broadband solid-state MAS NMR of paramagnetic systems. *Prog. Nucl. Magn. Reson. Spectrosc.* **2015**, *84−85*, 33−72.

(23) Edwards, J. W.; Speiser, R.; Johnston, H. L. Structure of Barium Titanate at Elevated Temperatures. *J. Am. Chem. Soc.* **1951**, *73*, 2934−2935.

(24) Grochala, W.; Edwards, P. P. Thermal Decomposition of the Non-Interstitial Hydrides for the Storage and Production of Hydrogen. *Chem. Rev.* **2004**, *104*, 1283−1316.

(25) Adam, J.; Klein, G.; Lehnert, T. Hydroxyl Content of BaTiO3Nanoparticles with Varied Size. *J. Am. Ceram. Soc.* **2013**, *96*, 2987−2993.

(26) Atakan, V.; Chen, C.-W.; Paul, R.; Riman, R. E. Quantification of Hydroxyl Content in Ceramic Oxides: A Prompt γ Activation Analysis Study of BaTiO3. *Anal. Chem.* **2008**, *80*, 6626−6632.

(27) Hennings, D.; Schreinemacher, S. Characterization of Hydrothermal Barium Titanate. *J. Eur. Ceram. Soc.* **1992**, *9*, 41−46.

(28) Abicht, H.-P.; Völtzke, D.; Schneider, R.; Woltersdorf, J.; Lichtenberger, O. Defect chemistry of the shell region of water-milled BaTiO3 powders. *Mater. Chem. Phys.* **1998**, *55*, 188−192.

(29) Pell, A. J.; Pintacuda, G.; Grey, C. P. Paramagnetic NMR in solution and the solid state, *Prog. Nucl. Magn. Reson. Spectrosc.* 2018, in press. DOI: 10.1016/j.pnmrs.2018.05.001

(30) McConnell, H. M.; Chesnut, D. B. Theory of Isotropic Hyperfine Interactions in π-Electron Radicals. *J. Chem. Phys.* **1958**, *28*, 107−117.

(31) Townes, C. H.; Herring, C.; Knight, W. D. The Effect of Electronic Paramagnetism on Nuclear Magnetic Resonance Frequencies in Metals. *Phys. Rev.* **1950**, *77*, 852−853.

(32) Ueda, T.; Hayashi, S.; Hayamizu, K. Hydrogen concentration dependence of 1H Knight shift in NbHx studied by 1H MAS NMR. *Solid State Commun.* **1993**, *87*, 429−434.

(33) Yesinowski, J. P. Solid-State NMR of Inorganic Semiconductors. *Top. Curr. Chem.* **2011**, *306*, 229−312.

(34) Bowman, R. C. NMR studies of electronic structure and hydrogen diffusion in transition metal hydrides. *Hyperfine Interact.* **1985**, *25*, 583−606.

(35) Yoo, H.-I.; Song, C.-R.; Lee, D.-K. BaTiO$_{3-\delta}$: Defect structure, electrical conductivity, chemical diffusivity, thermoelectric power, and oxygen nonstoichiometry. *J. Electroceram.* **2002**, *8*, 5−36.

(36) Schrader, M.; Mienert, D.; Oh, T.-S.; Yoo, H.-I.; Becker, K. D. An optical, EPR and electrical conductivity study of blue barium titanate, BaTiO3−δ. *Solid State Sci.* **2008**, *10*, 768−775.

(37) Kolodiazhnyi, T. Insulator-metal transition and anomalous sign several of the dominant charge carriers in perovskite BaTiO$_{3-\delta}$. *Phys. Rev. B: Condens. Matter Mater. Phys.* **2008**, *78*, 045107.

(38) Sinclair, D. C.; Skakle, J. M. S.; Morrison, F. D.; Smith, R. I.; Beales, T. P. Structure and electrical properties of oxygen-deficient hexagonal BaTiO3. *J. Mater. Chem.* **1999**, *9*, 1327−1331.

(39) Valdez-Nava, Z.; Tenailleau, C.; Guillemet-Fritsch, S.; El Horr, N.; Lebey, T.; Dufour, P.; Durand, B.; Chane-Ching, J.-Y. Structural characterization of dense reduced BaTiO3 and Ba0.95La0.05TiO3 nanoceramics showing colossal dielectric values. *J. Phys. Chem. Solids* **2011**, *72*, 17−23.

(40) Takeuchi, T.; Tabuchi, M.; Kageyama, H.; Suyama, Y. Preparation of Dense BaTiO3 Ceramics with Submicrometer Grains by Spark Plasma Sintering. *J. Am. Ceram. Soc.* **1999**, *82*, 939−943.